Volume 54
Number 30
14 August 2025
Pages 11453-11758

Dalton Transactions

An international journal of inorganic chemistry

rsc.li/dalton

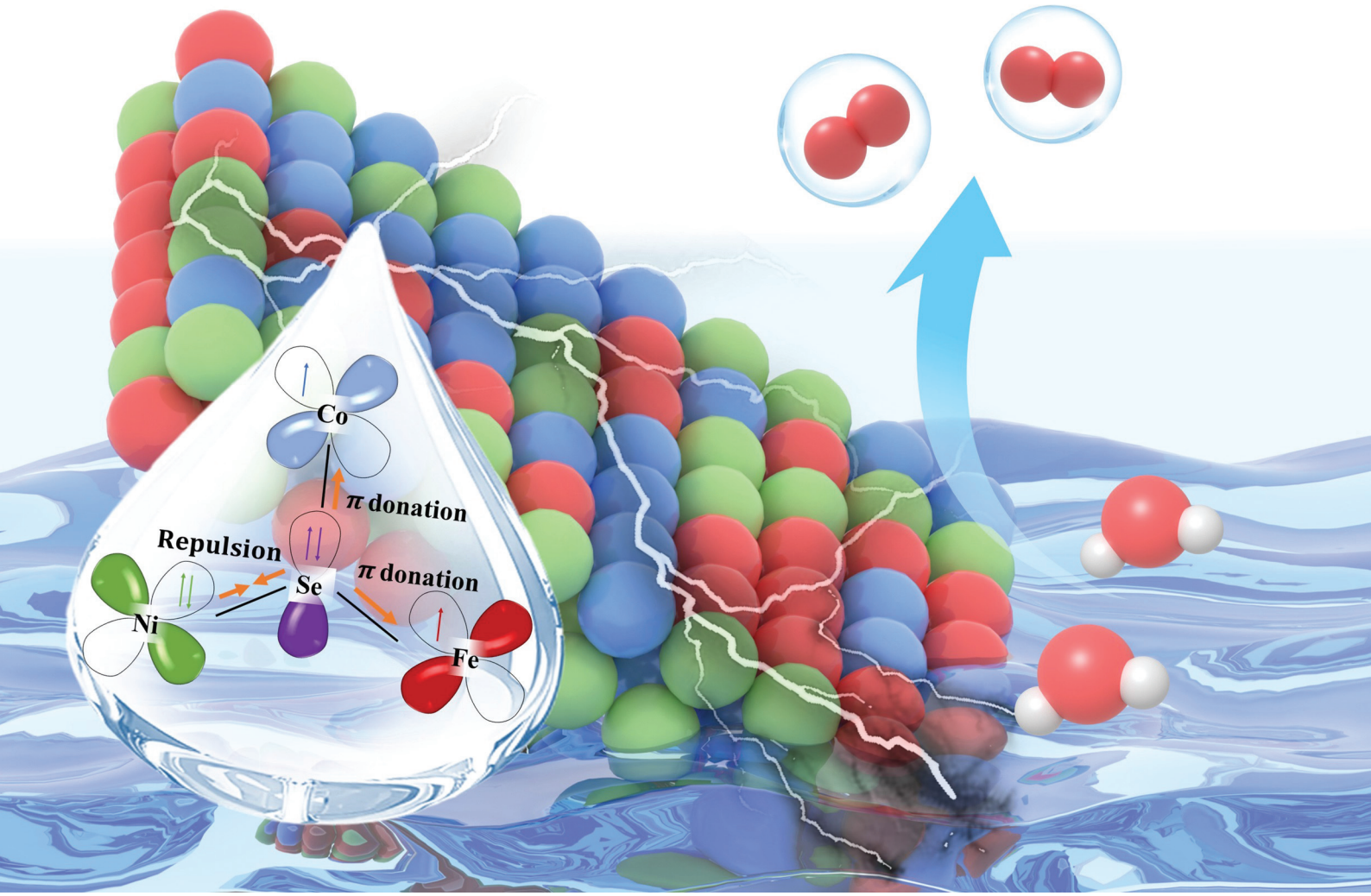

ISSN 1477-9226

ROYAL SOCIETY OF CHEMISTRY

PAPER

Xue-Zhi Song, Jing Liang, Xiao-Feng Wang, Zhenquan Tan *et al.*
Electronic structure regulation in medium-entropy CoNiFeSe enabling efficient and durable oxygen evolution electrocatalysis

Dalton Transactions

ROYAL SOCIETY OF CHEMISTRY

PAPER

View Article Online
View Journal | View Issue

Cite this: *Dalton Trans.*, 2025, **54**, 11516

Electronic structure regulation in medium-entropy CoNiFeSe enabling efficient and durable oxygen evolution electrocatalysis†

Yu-Xin Luan,‡ De-Kun Liu,‡ Yu-Xiang Chen, Xue-Zhi Song, * Jing Liang,* Xiao-Bing Wang, Wen-Qiang Sun, Yu-Lan Meng, Chen-Yu Shen, Ruichen Zhou, Jinxuan Liu, Xiao-Feng Wang * and Zhenquan Tan *

Received 27th March 2025,
Accepted 25th June 2025

DOI: 10.1039/d5dt00739a

rsc.li/dalton

Developing highly efficient and durable electrocatalysts for the oxygen evolution reaction (OER) holds great promise in revolutionizing the sustainable energy-conversion technologies, which greatly rely on the surface electronic structures. However, constructing catalytically active medium-entropy materials encounters great challenges due to the complex composition and the unsolved electronic structure–performance relationship. In this study, medium-entropy metal selenide (CoFeNiSe) with a cumulus-like architecture is fabricated through the selenylation of trimetallic hydroxide precursors. The medium-entropy CoFeNiSe manifests outstanding electrocatalytic OER activity and kinetics, that is, a low overpotential of 268 mV at 10 mA cm^{-2} and a Tafel slope of 53.33 mV dec^{-1} in 1 M KOH, outperforming the entropy-poor binary CoFeSe and CoNiSe, as well as its unary CoSe counterparts. It has been found experimentally and theoretically that the effective modulations of the valency and the d-band center at an optimal level regulate the adsorption/desorption ability of reaction intermediates *via* multimetallic electron interactions. This work provides valuable insight into the electronic structure regulation in entropy-rich materials, shedding light on the development of current green energy conversion technologies.

Introduction

The anxieties regarding the energy crisis and environmental pollution are becoming increasingly serious, brought about by large-scale fossil combustion.[1] Therefore, it is imminent to seek green and sustainable technologies for converting renewable electric energy into chemical fuels or storing it, achieving the long-term development of human society.[2,3] Fortunately, representative electrocatalytic technologies (water electrolysis, CO_2 reduction, metal–air batteries, *etc.*) provide solutions for sustainable energy utilization and have attracted intensive attention due to their mild operating conditions and carbon-free footprint.[4] The oxygen evolution reaction (OER) serving as the bottleneck in these promising energy vectors suffers from sluggish reaction kinetics, which requires cost-effective, highly active and robust electrocatalysts. However, the high cost and unsatisfactory durability greatly hinder the large-scale application of the most active Ru-/Ir-based materials.[5,6] Therefore, the exploration of superior electrocatalytic materials is the key to tackling the aforementioned issues and improving the energy conversion efficiency.

Numerous studies have witnessed that the design and preparation of Earth-abundant 3d-metal-based materials *via* controlling morphology and varying compositions, including metal hydroxides, metal phosphides, metal–organic frameworks, nitrides, *etc.*, can regulate their activity towards the OER.[7–15] Among these candidates, metal selenides show great superiority to other metal chalcogenides (*e.g.*, sulfides and oxides) in improving the catalytic activity for the OER due to the higher intrinsic electronic conductivity.[16–18] Researchers have developed various strategies to modulate the structures for further enhancing electrocatalytic performance. For example, seminal investigations demonstrated that the modulation of the metal to Se ratio in $NiSe_x$ and $CoSe_x$ would affect catalytic activity.[19,20] However, mono-metallic selenides face the dilemma of simple structures, untunable morphologies and limited ability to adjust the electronic structure. These issues can be overcome to some degree by constructing bi-metallic selenides or heterostructures, such as Fe doping in

Leicester International Institute, School of Chemical Engineering, Ocean and Life Sciences, School of General Education, State Key Laboratory of Fine Chemicals, Dalian University of Technology, 2 Dagong Road, Liaodongwan New District, Panjin, Liaoning 124221, China. E-mail: songxz@dlut.edu.cn, jingliang@mail.dlut.edu.cn, wangxf@dlut.edu.cn, tanzq@dlut.edu.cn

†Electronic supplementary information (ESI) available. See DOI: https://doi.org/10.1039/d5dt00739a

‡These authors contributed equally to this work.

NiSe or $MoSe_2$@$NiCo_2Se_4$ because of the synergistic effect between different metallic constituents.[21,22] Notwithstanding these achievements, it is still challenging to explore novel metal selenide-based electrocatalysts by exquisitely controlling the composition to engineer binding energy with intermediates accurately for efficient and durable electrocatalysis.

Since their discovery in 2004, high-entropy materials have emerged into a hotspot of electrocatalysis and shown great potential propelled by their core effects, that is, the high-entropy effect, the lattice distortion effect, the slow diffusion effect, and the cocktail effect.[23,24] These features and broad metal elements endow high-entropy materials with distorted lattice structures and excellent stability. Specifically, the random arrangement of multi-element atoms and the enhanced d–d interaction allow high-entropy materials for fine-tuning the electronic structure of active sites and desirable binding energy, providing a new solution to active electrocatalysis.[25–28] Under such circumstances, medium-entropy materials (MEMs) constituting four or fewer metallic components also have the above-mentioned merits, and MEMs will deliver enhanced catalytic activity when the size comes to the nanoscale.[29] Moreover, MEMs have great ease in optimizing the metal component and recovering metal species in comparison with their high-entropy counterparts, which is beneficial for industrial applications. Previous studies have introduced high entropy or medium entropy into metal selenides, including an $FeCoMnNiSe_2$ electrocatalyst on Ni foam, $(Ni,Fe,Co)Se_2$ nanosheets on a stainless steel mesh substrate and Ni–Co–Fe–Se@NiCo-LDH nanoarrays on Ni foam.[30–33] However, the exploration of advanced unsupported medium-entropy metal selenides comes across two obstacles: the miscibility of multi-elements partially inhibiting multiplicity synergies and the difficulty in deciphering the relationship between the electronic structure and activity. As a consequence, it is highly desirable to develop powerful methods to uniformly distribute metal components and investigate their electronic structure in depth.

In this work, one easily accessible approach was developed to fabricate homogeneous tri-metallic precursors. Then, the selenylation step was conducted under hydrothermal conditions to synthesize the medium-entropy CoFeNi selenide (CoNiFeSe). Significantly, the incorporation of Co, Ni and Fe elements adjusted the d-band center's position, thereby enhancing the catalytic OER activity of the newly designed medium-entropy CoNiFeSe material with an impressively low overpotential of 268 mV at 10 mA cm^{-2}. This work provides some fundamental insight into the electronic structure regulation for the electrocatalysts applied in water electrolysis.

Experimental section

Reagents and chemicals

The reagents used in the present work were all purchased from Tianjin Damao Corporation and Aladdin Corporation and used directly without any purification. They include metallic nitrates ($Co(NO_3)_2{\cdot}6H_2O$, $Fe(NO_3)_3{\cdot}9H_2O$ and $Ni(NO_3)_2{\cdot}6H_2O$), sodium borohydride ($NaBH_4$), sodium hypophosphite (NaH_2PO_2), hexadecyl trimethylammonium bromide (CTAB), potassium hydroxide (KOH, 85%), anhydrous ethanol and Se powder. Nafion solution in ethanol (5 wt%) was purchased from Aldrich Corporation as a binder for use. Water in the whole experiment was deionized before use.

Synthesis of materials

Synthesis of Co-LDH, CoNi-LDH, CoFe-LDH and CoNiFe-LDH. In the preparation of CoNiFe-LDH (LDH = layer double hydroxides), firstly, for solution A, 0.067 mmol of $Co(NO_3)_2{\cdot}6H_2O$ (15.6 mg), 0.067 mmol of $Fe(NO_3)_3{\cdot}9H_2O$ (21.7 mg), and 0.067 mmol of $Ni(NO_3)_2{\cdot}6H_2O$ (15.6 mg) (with a molar ratio of 1 : 1 : 1, total number of moles of 2 mmol) were dissolved in 15 mL of deionized water. For solution B, 500 mg of CTAB was dissolved in 10 mL of deionized water. Then solution B was dropwise added into solution A with continuous stirring.

In the second step, for solution C, 100 mg of $NaBH_4$ was dissolved in 10 mL of deionized water. Solution C was slowly added dropwise into the mixed solution and continuously stirred for 30 min. Then the final suspension was centrifuged and the products were washed with deionized water twice and anhydrous ethanol once and then dried at 60 °C.

For the preparation of comparable CoNi-LDH, CoFe-LDH, and Co-LDH materials, the initial solutes in solution A were different from those in CoNiFe-LDH, which were $Co(NO_3)_2{\cdot}6H_2O$ (1.00 mmol) and $Ni(NO_3)_2{\cdot}6H_2O$ (1.00 mmol) for CoNi-LDH, $Co(NO_3)_2{\cdot}6H_2O$ (1.00 mmol) and $Fe(NO_3)_3{\cdot}9H_2O$ (1.00 mmol) for CoFe-LDH, and $Co(NO_3)_2{\cdot}6H_2O$ (2.00 mmol) for Co-LDH. The other procedures are identical to the preparation of CoNiFe-LDH.

Synthesis of CoSe, CoNiSe, CoFeSe and CoNiFeSe. In the preparation of CoNiFeSe, for suspension A, 20 mg CoNiFe-LDH was dispersed in 4 mL of deionized water. For solution B, 22.5 mg $NaBH_4$ was dissolved in 6 mL of deionized water and then 20 mg Se powder was added under constant stirring until Se powder was totally dissolved. Solution B was added rapidly into solution A and stirred for 10 min. The final suspension was transferred to a Teflon-lined autoclave and heated to 100 °C for 4 h. After cooling it naturally, the final products were rinsed with anhydrous ethanol and then dried at 60 °C. The procedures for the synthesis of CoNiSe, CoFeSe and CoSe were similar to the preparation of CoNiFeSe by using CoNi-LDH, CoFe-LDH and Co-LDH as the corresponding materials.

Characterization

Scanning electron microscopy (SEM) images were captured using an FEI Nova Nano SEM 450 field emission scanning electron microscope. Transmission electron microscopy (TEM), high-resolution TEM (HRTEM), selected area electron diffraction (SAED) and energy dispersive X-ray spectroscopy (EDX) mapping images were recorded using a Tecnai G2 F30 microscope from FEI Corporation. A powder polycrystalline X-ray diffractometer (XRD) using model 7000S from

Shimadzu Corporation (Cu Kα radiation source, wavelength: 1.5406 Å) was employed to qualitatively analyze the crystallinity and purity of the material. The XRD measurements were performed in the 2θ range of 5–80° at a voltage of 40 kV and a current of 40 mA. Additionally, X-ray photoelectron spectroscopy (XPS) measurements were conducted to record the surface chemistry and valence band spectra on an ESCALABTM 250Xi spectrometer (Al Kα radiation source, $h\nu$ = 1486.68 eV).

Electrochemical measurements

All electrochemical measurements were carried out in a three-electrode cell on a CHI660E electrochemical workstation (Shanghai Chenhua Instrument Corporation, China) using the glassy carbon electrode as the working electrode (a radius of 5 mm), Hg/HgO as the reference electrode, and a platinum sheet as the counter electrode at room temperature. The working electrode was prepared as follows: 480 μL of ethanol and 480 μL of deionized water were added to 4 mg of the sample to be tested, and 40 μL of Nafion reagent was added to the sample, and then the mixture was ultrasonicated to make it uniformly dispersed. Then 8 μL of the solution was taken once and dropped twice on the glassy carbon electrode to ensure uniform coverage, followed by drying. After drying, the electrolyte was tested with 1 M KOH electrolyte. The scan rate of linear sweep voltammetry (LSV) was 5 mV s^{-1} without an *iR* compensation. All potentials in this work were corrected to a reversible hydrogen electrode (RHE) as follows: $E_{RHE} = E_{Hg/HgO} + 0.0592\ V \times pH + 0.098\ V$. Overpotentials were obtained using the following equation: $\eta = E_{RHE} - 1.23$ V. Then the Tafel slope was obtained from the conversion from the LSV curves and subsequent fitting. Cyclic voltammetry (CV) curves were recorded at a scan rate from 20 mV s^{-1} to 120 mV s^{-1} with a potential range of 0.2–0.3 V *versus* Hg/HgO to calculate the double layer capacitance (C_{dl}) for the OER, respectively. Electrochemical impedance spectra (EIS) were recorded over a frequency range of 10^5–0.01 Hz at a potential of 0.583 V (*vs.* Hg/HgO) with an AC amplitude of 5 mV. The long-term stability of the catalyst-loaded working electrode prepared by loading CoNiFeSe on carbon paper (1 mg cm^{-2}) was tested with chronoamperometry.

Results and discussion

As shown in Scheme 1, there are two main steps in the synthesis process of medium-entropy CoNiFeSe materials: the presynthesis and selenization treatment of CoNiFe-LDH precursors. The CoNiFe-LDH precursors were prepared by our developed reduction–hydrolysis tactics under surfactant modulation with crucial $NaBH_4$ to simultaneously provide an alkaline and reductive environment, and the selenization treatment was conducted under hydrothermal conditions.[34,35] Both these steps can be operated in a simple manner and are time-efficient, providing great ease to fabricate the functional medium-entropy CoNiFeSe materials.

The morphologies of the as-synthesized LDH-based precursors and metal selenide materials were characterized using SEM. The as-synthesized CoNiFe-LDH displayed uniform sakura-like morphology with abundant nanosheets as petals assembling together with a diameter of about 100–200 nm (Fig. 1a and b). Moreover, the metallic compositions in different LDH-based precursors also exert a profound effect on their morphologies, in which the morphology of CoNi-LDH (Fig. S1a and b†) is similar to that of CoNiFe-LDH. For Co-LDH, the lateral size becomes much larger, which is similar to the surface of a cocoon (Fig. S2a and b†). But the CoFe-LDH shows coralline-like morphology (Fig. S3a and b†). After the selenization treatment of CoNiFe-LDH, CoNiFeSe basically retains the initial state of CoNiFe-LDH and further reveals a cumulus-like architecture (Fig. 1c and d). The cumulus-like

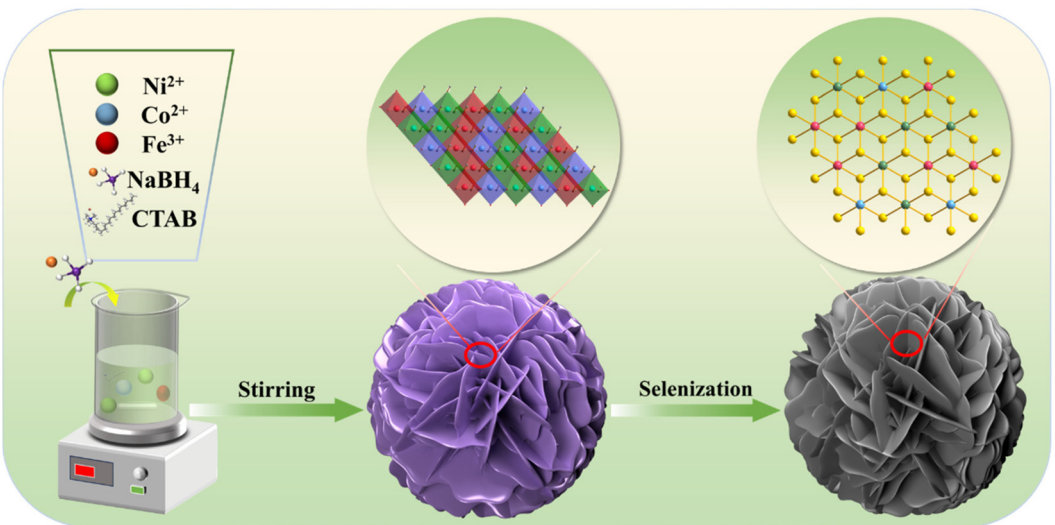

Scheme 1 Schematic illustration for the synthesis of CoNiFeSe.

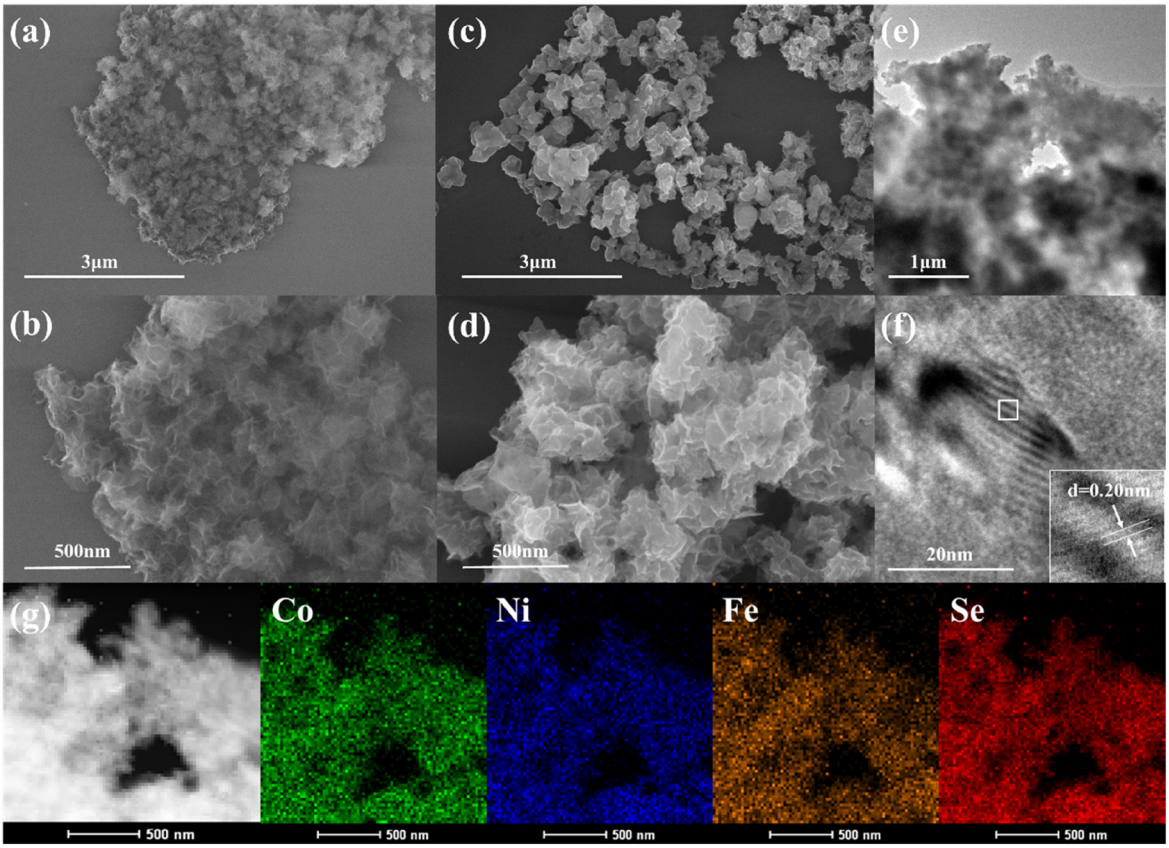

Fig. 1 (a and b) SEM images of CoNiFe-LDH, (c and d) SEM images of CoNiFeSe, (e) TEM of CoNiFeSe, (f) HRTEM image of CoNiFeSe, and (g) HAADF-STEM image, and the corresponding EDS mapping images of CoNiFeSe.

architecture features uniform particle morphology with visible interconnections originating from the flowerlike CoNiFe-LDH. The TEM image in Fig. 1e reveals that CoNiFeSe exhibits a clustered structure formed by ultrathin nanosheets as building blocks, leaving some pores. These special morphological features, such as nanosheets and pores, would expose more active catalytic sites on the material's surface and enable better electrolyte diffusion, faster charge transfer, and efficient removal of gases generated during the catalytic reaction, ultimately contributing to superior OER catalytic performance. The high-resolution TEM (HRTEM) image in Fig. 1f displays lattice spacings of 0.203 nm, corresponding to the (102) plane of FeCoNiSe (PDF#52-1008). The SAED image showing a set of diffraction rings suggests a polycrystalline diffraction pattern (Fig. S4†).[36] The prominent diffraction rings observed in the SAED pattern can be assigned to the (101), (103), and (202) planes of $Co_{0.85}Se$ (JCPDS: 52-1008), supporting the successful formation of CoNiFeSe with homogeneous mixed metallic elements. Furthermore, high-angle annular dark-field scanning transmission electron microscopy (HAADF-STEM) images and EDS elemental mapping images illustrate a uniform distribution of Fe, Co, Ni and Se throughout the CoNiFeSe structure (Fig. 1g). The uniform distribution with an almost equal atomic content of Co, Ni and Fe (Fig. S5†) fosters a synergistic interaction among the multiple elements to regulate the electronic structure, further boosting conductivity and improving oxygen adsorption/desorption capabilities, both of which positively contribute to the electrochemical catalytic performance.[37] According to the EDS results, the calculated ΔS_{mix} of the CoNiFeSe material is 1.08R, which confirms its medium-entropy characteristic.

To further confirm the crystallographic feature of the as-synthesized metal selenides, powder XRD measurement was performed and the corresponding patterns are compiled in Fig. 2a. The diffractions of CoNiFeSe, CoNiSe, CoFeSe and CoSe basically match the simulated ones in $Co_{0.85}Se$ (JCPDS 52-1008). In the case of CoNiFeSe, it is clear that the reflections at 2θ being 33.26°, 44.74°, and 50.56° were attributed to the (101), (102), and (110) crystal planes of $Co_{0.85}Se$ (JCPDS 52-1008), which agrees with the SAED result above. In comparison with unary CoSe, a slight negative shift to the low diffraction angle direction is observed in binary CoFeSe. This shift is likely caused by the replacement of Co ions with larger Fe ions, increasing the lattice constant and decreasing the 2θ value according to the Bragg equation ($2d \sin\theta = n\lambda$). The Ni-containing materials, such as CoNiSe and CoNiFeSe, show enhanced crystallinity, which may illustrate Ni doping significantly endowing the strong synergistic effect among different centers in ternary metallic selenides.[38]

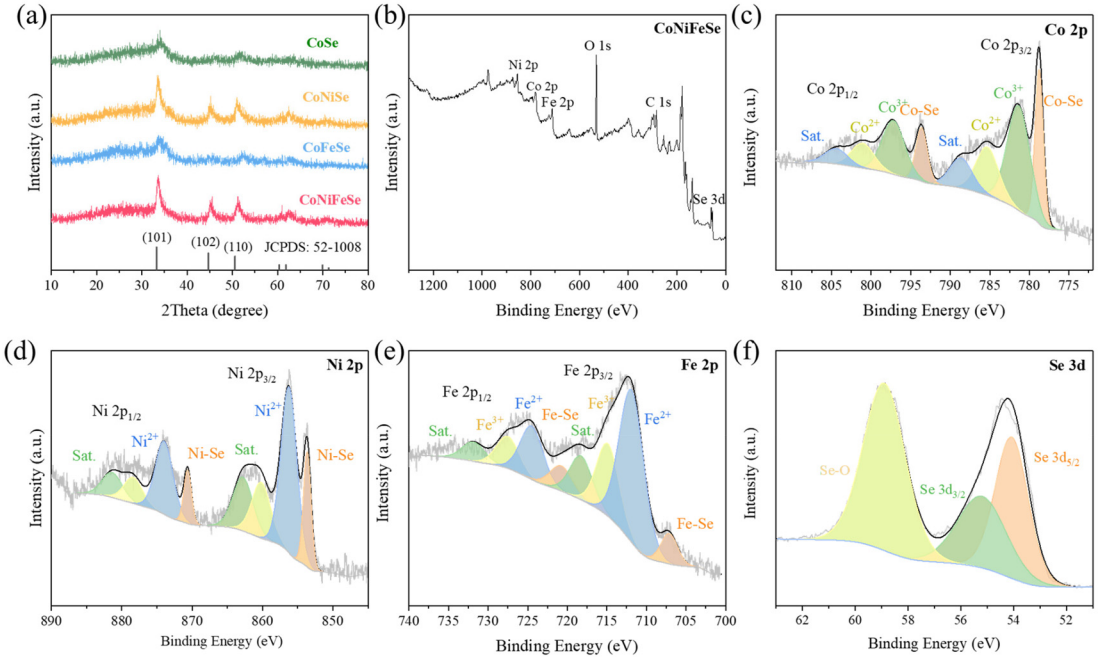

Fig. 2 (a) XRD of CoNiFeSe, CoFeSe, CoNiSe and CoSe, (b) full XPS spectrum, (c) Co 2p spectrum, (d) Ni 2p spectrum, (e) Fe 2p spectrum, and (f) Se 3d spectrum of CoNiFeSe.

The full XPS spectrum of CoNiFeSe shown in Fig. 2b shows the presence of Ni 2p, Co 2p, Fe 2p, O 1s and Se 3d. The Co 2p XPS spectrum reveals four distinct $2p_{3/2}$ peaks and four $2p_{1/2}$ peaks (Fig. 2c). These peaks in the $2p_{3/2}$ region include the peak at 778.75 eV which can be attributed to the Co–Se bond, the peak at 781.45 eV which can be assigned to high-valence Co^{3+}, the intermediate state $Co^{2+}$and the satellite peaks located at 785.45 eV and 788.52 eV. There are also four corresponding peaks in the $2p_{1/2}$ region.[39,40] The Ni $2p_{3/2}$ spectrum of Fig. 2d can be deconvoluted into two components: one at 853.5 eV, accompanied by a satellite peak, corresponding to the Ni–Se bond in CoNiFeSe, and the other at 856.5 eV, with a satellite peak being attributed to Ni^{2+}.[41] In the Fe 2p region of CoNiFeSe, as depicted in Fig. 2e, the binding energy at 707.20 eV is assigned to the Fe–Se bond, aligning with previous studies.[38] Additionally, two peaks at 711.52 eV and 724.80 eV, along with their satellite peaks, correspond to Fe $2p_{3/2}$ and Fe $2p_{1/2}$ of the Fe–O bond, respectively.[38,42] The high-resolution Se 3d XPS spectrum can be deconvoluted into three distinct peaks (Fig. 2f). The two primary peaks at binding energies of 53.85 eV and 55.35 eV correspond to the Se $3d_{5/2}$ and Se $3d_{3/2}$ spin–orbit components, respectively. These binding energies are characteristic of selenium in the −2 oxidation state, indicating that the selenium in the CoNiFeSe compound exists predominantly as Se^{2-}. Additionally, the broad peak observed at 59.40 eV can be attributed to the presence of the oxidized Se species, indicating that the surface of selenides may be oxidized in the air.[43,44]

The electrocatalytic performance of the OER of the selenides was studied by linear sweep voltammetry (LSV) under the conditions of a typical three-electrode system using 1.0 M KOH as the electrolyte. Fig. 3a shows the LSV curves of CoNiFeSe, CoFeSe, CoNiSe and CoSe, respectively. The CoNiFeSe material can drive an earliest current response at 1.33 V (*vs.* RHE), and the current will dramatically increase when the anodic applied potential is increased. The overpotentials to attain a density of 10 mA cm^{-2} were 268 mV for CoNiFeSe, 307 mV for CoFeSe, 356 mV for CoNiSe and 338 mV for CoSe, respectively (Fig. 3b). Clearly, the overpotential of CoNiFeSe is much smaller than others, which proves that this medium-entropy catalyst has excellent electrocatalytic activity. OER kinetics was studied by extracting the Tafel slope from the LSV curve, since the value of the Tafel slope is a key parameter to reveal the OER kinetics. As illustrated in Fig. 3c, the Tafel slope value of CoNiFeSe is 53.33 mV dec^{-1}, which is smaller than CoFeSe (57.04 mV dec^{-1}), CoNiSe (89.26 mV dec^{-1}) and CoSe (88.55 mV dec^{-1}), revealing the favorable kinetics accelerated by trimetallic components. We also evaluated the impressive CoNiFeSe material against other reported materials, including but not limited to high/medium-entropy materials and metal selenides, based on overpotential at a current of 10 mA cm^{-2} and the Tafel slope (Table S1†). Notably, its performance either matches or exceeds that of many reported materials, such as $Ni(CN)_2/NiSe_2$, $(NiFeCoMn)_3S_4$ and Ni@Co/Se_2 or NiFe-Se/CFP.[45–48]

The electrochemically active surface area (ECSA) indicates the density of electrochemically active sites present per unit area of the catalyst material. The double-layer capacitance (C_{dl}), derived from cyclic voltammetry (CV) curves at varying scan rates, is directly proportional to the ECSA.[49] The magni-

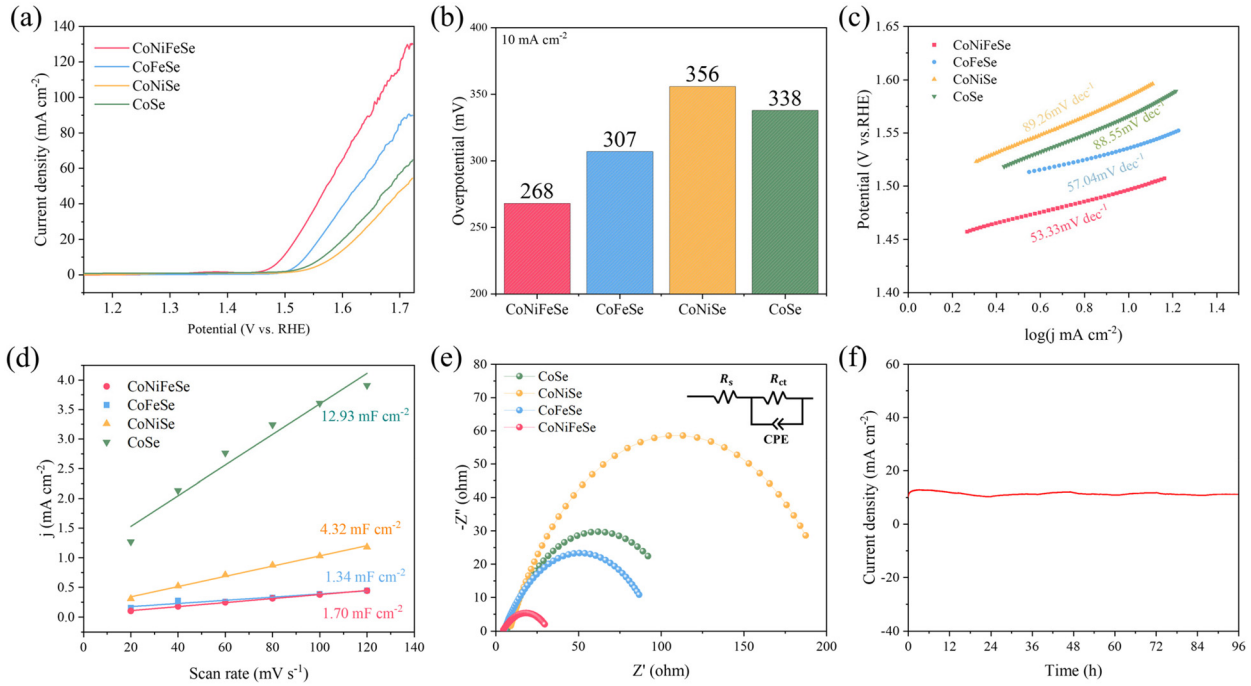

Fig. 3 (a) LSV curves, (b) overpotentials at 10 mA cm^{-2}, (c) Tafel curves, (d) the current anodic–cathodic difference in CV curves, (e) the fitted Nyquist plots of CoNiFeSe, CoFeSe, CoNiSe and CoSe with an equivalent circuit inset, and (f) long-term stability of CoNiFeSe.

tude of C_{dl} serves as an indicator of the quantity of electrochemically active sites available. CVs were collected at sweep rates of 20 mV s^{-1}, 40 mV s^{-1}, 60 mV s^{-1}, 80 mV s^{-1}, 100 mV s^{-1} and 120 mV s^{-1} for 40 consecutive cycles and are shown in Fig. S6.† The C_{dl} is calculated by the capacitive current difference (Δj) at different scan rates in the non-faradaic region. The C_{dl} of CoNiFeSe is 1.70 mF cm^{-2}, CoFeSe is 1.34 mF cm^{-2}, CoNiSe is 4.32 mF cm^{-2} and CoSe is 12.93 mF cm^{-2}, revealing that uni-metallic CoSe possesses a large number of active sites (Fig. 3d). And the decreased active site number may be related to the micromorphology change caused by the introduction of one or two extra metallic components. The distinguished electrocatalytic activity and the limited active site of CoNiFeSe provide a hint that other factors may determine the final activity. To further understand the OER performance of the polymetallic selenides, electrochemical impedance spectroscopy (EIS) was conducted to analyze the charge transfer behavior at the interface between the electrolyte and the catalyst surface, covering a wide frequency range from 100 000 Hz to 0.01 Hz. The radius of curvature in this context is directly related to the charge transfer resistance and inversely related to the charge transfer capacity. The Nyquist plots recorded for the CoNiFeSe, CoFeSe, CoNiSe and CoSe catalysts are shown in Fig. 3e with an equivalent circuit. The CoNiFeSe electrode has an R_{ct} value of 30.52 Ω, smaller than CoSe (110.70 Ω), CoFeSe (92.23 Ω), and CoNiSe (202.50 Ω). It proves that CoNiFeSe has the lowest charge transfer resistance, which is in good agreement with the LSV trend above. The exceptional durability of the polymetallic catalyst is essential for sustainable energy-related electrocatalytic applications. The CoNiFeSe catalyst remained stable for 96 hours (Fig. 3f)with a good retention of the initial current density of 10 mA cm^{-2}, which underscores its excellent stability. After the electrocatalytic stability test, the recorded XPS spectra of Co, Ni, and Fe changed significantly in comparison with their initial states (Fig. S9–11†). After the stability test, the Co 2p XPS spectrum showed the disappearance of Co–Se bonds and the formation of CoOOH, which may serve as the primary active phase.[44,50] The HRTEM image of CoNiFeSe after the stability test reveals the formation of amorphous CoOOH on the outer layer with the retention of metal selenides inside (Fig. S12†). The Raman spectrum of CoNiFeSe after the electrochemical stability test also indicates the formation of an active MOOH phase (Fig. S13†).

To further elucidate the mechanism of the activity enhancement in medium-entropy CoNiFeSe, a set of analyses and investigations were conducted. The ECSA-normalized current curves presented in Fig. S14† clearly demonstrate the much larger current density of CoNiFeSe than other counterparts, which reveals that the medium-entropy CoNiFeSe has the largest intrinsic activity at each active site. To the best of our knowledge, the intrinsic per-site activity is relevant to the electronic structure of the active site. Then, the XPS spectra of different materials have been compiled and compared in Fig. 4a to clarify the electronic structure modulated effect. The four materials show similar deconvoluted peaks, with Co–Se peaks, Co^{3+}/Co^{2+} peaks and satellite peaks. The area ratio of the Co–Se bond basically increases from unary CoSe to the target ternary CoNiFeSe material, indicating the stabilization

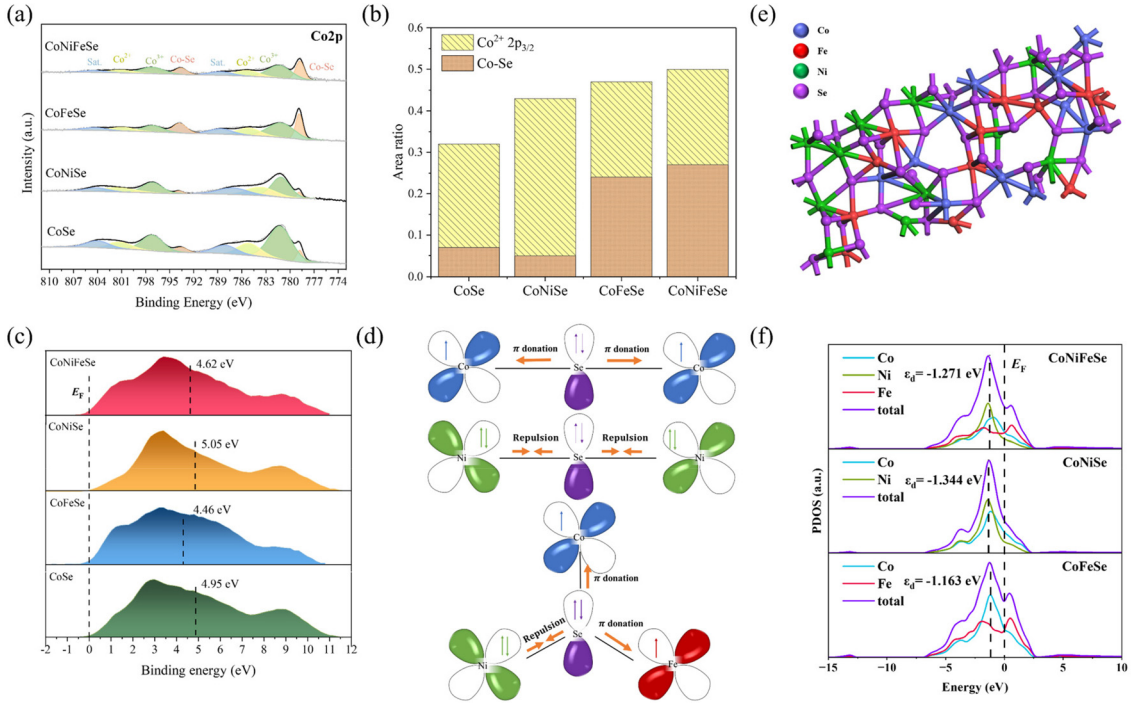

Fig. 4 (a) Co 2p spectra of CoNiFeSe, CoFeSe, CoNiSe and CoSe, (b) the comparison of Co 2p XPS spectra for CoNiFeSe, CoFeSe, CoNiSe and CoSe, (c) valence band spectra of CoNiFeSe, CoFeSe, CoNiSe and CoSe, (d) schematic diagram of electronic coupling of Co, Ni, Fe and Se, (e) the structure model of CoNiFeSe, and (f) the PDOS of CoNiSe, CoFeSe and CoNiFeSe.

effect on Co–Se species induced by the entropy increase (Fig. 4b). And the content of the easily oxidized species including Co–Se and Co^{2+} may endow the material with more active sites, possibly improving the activity for the OER.[51,52]

Based on the well-established d-band theory, the d-band center (E_d) serves as a valuable descriptor for examining the interactions between metal sites on the catalyst surface and oxygen-related intermediates.[53] On the basis of valence band spectrum analysis among the materials studied (Fig. 4c), the E_d energy levels were calculated. The introduction of individual Ni species would downshift the d-band from CoSe (4.95 eV) to CoNiSe (5.05 eV). This d-band shift would lead to weak bonding to the reaction intermediates, hindering their adsorption on the CoNiSe and CoSe. Conversely, the d-band manifests an upward shift when the single Fe element is introduced to CoSe, with a d-band center of 4.46 eV in CoFeSe. The elevated E_d energy level relative to the Fermi level raises the antibonding states and reduces the occupancy of the antibonding state, resulting in overly tight bonding between the metal sites and intermediates.[54] The medium-entropy CoNiFeSe material possesses an optimized E_d energy level (4.62 eV), which allows it to effectively balance the adsorption and desorption processes of OH*, O*, and OOH* intermediates on its metal sites, thereby improving its electrocatalytic OER performance.[55,56] The electronic structure modulation is directly related to the charge transfer and electronic interactions, which can be elucidated in terms of the valence electron structure on the basis of XPS results. In this context, the M–Se–M bonding (where M = Co or Fe) is used to describe the electron interactions between transition metal elements. As illustrated in Fig. 4d, the unpaired electron in the π-symmetry (t_{2g}) d-orbitals of Co and Fe cations can only achieve a weak electron interplay *via* an Se bridge with π donation features. The two Ni^{2+} ($t_{2g}^6e_g^2$) ions have fully occupied π-symmetry (t_{2g}) d-orbitals, leading to strong electron–electron repulsion between Se^{2-} and Ni^{2+} ions.[57,58] After coupling Co, Ni and Fe cations, the simultaneous e^-–e^- repulsion and π-donation would trigger the modulation of the electronic structure of the metal center, being conducive to efficient OER elelctrocatalysis.[59]

To further explore the inherent electronic effect in medium-entropy CoNiFeSe, density functional theory (DFT) calculations were performed in this work. The structure of medium-entropy CoNiFeSe (102) was constructed for calculation in Fig. 4e, while CoNiSe (102) and CoFeSe (102) structures are shown in Fig. S16 and S17.† The projected density of states (PDOS) for different materials was calculated and is compiled in Fig. 4f. Then, the d-band centers of CoNiFeSe, CoNiSe and CoFeSe are determined to be −1.271 eV, −1.344 eV and −1.163 eV, respectively. The theoretical d-band center order is in good agreement with the experimental XPS valence band spectrum analysis. These results further demonstrate that the medium-entropy CoNiFeSe material exhibits moderate intermediate adsorption strength by the synergistic Ni and Fe electronic modulated effect, with the adsorption strength order of CoFeSe > CoNiFeSe > CoNiSe.

Conclusions

In summary, this work demonstrated a facile two-step route toward the fabrication of a medium-entropy CoNiFeSe material with a cumulus-like architecture through the preparation of LDH precursors by reduction–hydrolysis and hydrothermal selenization processes. The medium-entropy CoNiFeSe electrocatalyst displays an overpotential as low as 268 mV for the alkaline OER. Experimental findings demonstrated that the electronic interaction within the medium-entropy CoNiFeSe material facilitates charge transfer and precisely regulates the d-band center for optimizing the adsorption ability of intermediates, thereby significantly improving the intrinsic per-site activity. In addition, this electrocatalyst also exhibits long-term outstanding stability. This work would pave the way to the exploration of medium-entropy electrocatalysts on the basis of multi-site synergistic electronic interactions for practical OER-related energy conversion technologies.

Conflicts of interest

There are no conflicts to declare.

Author contributions

Yu-Xin Luan: synthesis, characterization, catalytic activity assay, writing – original draft and revision. De-Kun Liu: theoretical calculation and revision. Yu-Xiang Chen: drawing pictures and analysis. Xue-Zhi Song: supervision, data analysis, funding, and review and editing. Jing Liang: supervision, review and editing. Xiao-Bing Wang: structure characterization. Wen-Qiang Sun: materials synthesis methods. Yu-Lan Meng: writing, review and editing. Chen-Yu Shen and Ruichen Zhou: catalytic activity test. Jinxuan Liu: editing and review. Xiao-Feng Wang: editing and review. Zhenquan Tan: funding, supervision and methodology.

Data availability

Data will be made available on request.

Acknowledgements

We are grateful for the financial support from the National Natural Science Foundation of China (No. 22271036), the Natural Science Foundation of Liaoning Province of China (No. 2024-MSBA-17 and 2023-MSBA 012), the Fundamental Research Funds for the Central Universities of China (DUT24MS012, DUT23BK031, DUT24BK038 and DUT24BK078), and the Open Research Fund of Guangdong Advanced Carbon Materials Co., Ltd (Kargen 2024B0802).

References

1 P. Achakulwisut, P. Erickson, C. Guivarch, R. Schaeffer, E. Brutschin and S. Pye, *Nat. Commun.*, 2023, **14**, 15.
2 S. Chu, Y. Cui and N. Liu, *Nat. Mater.*, 2017, **16**, 16–22.
3 W. Dong, H. Xiao, Y. Jia, L. Chen, H. Geng, S. U. H. Bakhtiar, Q. Fu and Y. Guo, *Adv. Sci.*, 2022, **9**, 2105368.
4 S. Li, M. Zhao, Z. Wang, Z. Zhang, Z. Yan and X. Xiao, *Ionics*, 2023, **29**, 3225–3236.
5 H. Huang, L. Fu, W. Kong, H. Ma, X. Zhang, J. Cai, S. Wang, Z. Xie and S. Xie, *Small*, 2022, **18**, 2201333.
6 M. Huang, H. Yang, X. Xia and C. Peng, *Appl. Catal., B*, 2024, **358**, 124422.
7 Y. Chen, C. Qiu, Z. Zou, Y. Ling, F. Gao, Y. Shao and Q. Wang, *Electrochim. Acta*, 2022, **426**, 140773.
8 S. A. Khalate, S. A. Kadam, Y.-R. Ma, S. B. Kulkarni, V. G. Parale and U. M. Patil, *J. Colloid Interface Sci.*, 2022, **613**, 720–732.
9 G. Li, P. Wang, C. Li, Z. Fang, M. He, W. Wang, X. Yuan, H. Li, P. Li and Z. Li, *Mater. Res. Lett.*, 2022, **10**, 744–753.
10 L. Zhi, J. Tu, J. Li, M. Li and J. Liu, *J. Colloid Interface Sci.*, 2022, **616**, 379–388.
11 C. Wang, Z. Wang, Z. Yao, H. Liu, X. Li, M. L. K. Essandoh, P. Dong, M. Ye and J. Shen, *Dalton Trans.*, 2022, **51**, 6654–6662.
12 X. Chen, Z. Qiu, H. Xing, S. Fei, J. Li, L. Ma, Y. Li and D. Liu, *Appl. Catal., B*, 2022, **305**, 121030.
13 D. Lai, Q. Kang, F. Gao and Q. Lu, *J. Mater. Chem. A*, 2021, **9**, 17913–17922.
14 X. Xu and T. Yu, *Dalton Trans.*, 2025, **54**, 3393–3400.
15 K. Sanket, U. Kumar, I. Sinha and S. K. Behera, *Dalton Trans.*, 2025, **54**, 797–810.
16 H. Wu, Z. Wang, Z. Li, Y. Ma, F. Ding, F. Li, H. Bian, Q. Zhai, Y. Ren, Y. Shi, Y. Yang, Y. Deng, S. Tang and X. Meng, *Adv. Energy Mater.*, 2023, **13**, 2300837.
17 Y. Huang, L.-W. Jiang, B.-Y. Shi, K. M. Ryan and J.-J. Wang, *Adv. Sci.*, 2021, **8**, 2101775.
18 J. Yuan, X. Cheng, H. Wang, C. Lei, S. Pardiwala, B. Yang, Z. Li, Q. Zhang, L. Lei, S. Wang and Y. Hou, *Nano-Micro Lett.*, 2020, **12**, 104.
19 S. Anantharaj, E. Subhashini, K. C. Swaathini, T. S. Amarnath, S. Chatterjee, K. Karthick and S. Kundu, *Appl. Surf. Sci.*, 2019, **487**, 1152–1158.
20 Y. Zhao, B. Jin, Y. Zheng, H. Jin, Y. Jiao and S.-Z. Qiao, *Adv. Energy Mater.*, 2018, **8**, 1801926.
21 Z.-P. Wu, H. Zhang, S. Zuo, Y. Wang, S. L. Zhang, J. Zhang, S.-Q. Zang and X. W. Lou, *Adv. Mater.*, 2021, **33**, 2103004.
22 A. Majumdar, P. Dutta, A. Sikdar, H. Lee, D. Ghosh, S. N. Jha, S. Tripathi, Y. Oh and U. N. Maiti, *Small*, 2022, **18**, 2200622.
23 X. Yan, Y. Zhou and S. Wang, *Adv. Funct. Mater.*, 2025, **35**, 2413115.
24 J.-C. Ni, Y.-X. Luan, X.-F. Wang, Z. Tan and X.-Z. Song, *J. Mater. Chem. A*, 2024, **12**, 14268–14301.

25 T. A. A. Batchelor, J. K. Pedersen, S. H. Winther, I. E. Castelli, K. W. Jacobsen and J. Rossmeisl, *Joule*, 2019, **3**, 834–845.
26 L. Wang, H. Su, Z. Zhang, J. Xin, H. Liu, X. Wang, C. Yang, X. Liang, S. Wang, H. Liu, Y. Yin, T. Zhang, Y. Tian, Y. Li, Q. Liu, X. Sun, J. Sun, D. Wang and Y. Li, *Angew. Chem., Int. Ed.*, 2023, **62**, e202314185.
27 J. Tian, Y. Rao, W. Shi, J. Yang, W. Ning, H. Li, Y. Yao, H. Zhou and S. Guo, *Angew. Chem., Int. Ed.*, 2023, **62**, e202310894.
28 J. Zhu, J. Chen, X. Li, K. Luo, Z. Xiong, Z. Zhou, W. Zhu, Z. Luo, J. Huang and Y. Li, *J. Energy Chem.*, 2024, **92**, 383–393.
29 J. Yuan, Q. Qi, Q. Wan, J. Gong, Y. Zhang, Y. Feng, C. Zhang and J. Hu, *Dalton Trans.*, 2025, **54**, 5293–5300.
30 Z. Liu, X. Guo, T. Cui, S. Mu, Z. Ni, C. Zhang and S. Lu, *J. Power Sources*, 2024, **592**, 233956.
31 J. Zhang, S. Zhang, Z. Zhang, J. Wang, Z. Zhang and G. Cheng, *J. Alloys Compd.*, 2023, **939**, 168753.
32 Z. Dai, X. Du and X. Zhang, *J. Alloys Compd.*, 2023, **946**, 169451.
33 J. Dang, J. Qiu, X. Zhang and J. Zhang, *Dalton Trans.*, 2025, **54**, 1468–1475.
34 X.-Z. Song, W.-Y. Zhu, J.-C. Ni, Y.-H. Zhao, T. Zhang, Z. Tan, L.-Z. Liu and X.-F. Wang, *ACS Appl. Mater. Interfaces*, 2022, **14**, 33151–33160.
35 X.-Z. Song, X.-B. Wang, T. Zhang, J.-H. Dong, Y.-L. Meng, D.-K. Liu, Y.-X. Luan, C. Yao, Z. Tan and X.-F. Wang, *ACS Appl. Mater. Interfaces*, 2024, **16**, 55248–55257.
36 L. Zhao, J. Zhang, G. Jin, Z.-J. Jiang and Z. Jiang, *J. Colloid Interface Sci.*, 2024, **668**, 525–539.
37 S. Bai, W. Dai, X. Yang, B. Wu, J. Guo, C. Zhao, Y. Zhang, C. Cui, G. Zou and S. Huang, *Int. J. Hydrogen Energy*, 2024, **84**, 615–622.
38 C. Liu, Y. Han, L. Yao, L. Liang, J. He, Q. Hao, J. Zhang, Y. Li and H. Liu, *Small*, 2021, **17**, 2007334.
39 Z. Jiang, Y. Yuan, L. Tan, M. Li and K. Peng, *Appl. Surf. Sci.*, 2023, **627**, 157282.
40 H. Liang, L. Jia, F. Chen, S. Jing and P. Tsiakaras, *Appl. Catal., B*, 2022, **317**, 121698.
41 I. Pathak, S. Prabhakaran, D. Acharya, K. Chhetri, A. Muthurasu, Y. R. Rosyara, T. Kim, T. H. Ko, D. H. Kim and H. Y. Kim, *Small*, 2024, **20**, 2406732.
42 N. S. McIntyre and D. G. Zetaruk, *Anal. Chem.*, 1977, **49**, 1521–1529.
43 J. Zheng, X. Li, C. He, C. Zhou, H. Zhang, B. Tang and Y. Rui, *ChemElectroChem*, 2020, **7**, 782–791.
44 X. Xu, F. Song and X. Hu, *Nat. Commun.*, 2016, **7**, 12324.
45 J. Nai, X. Xu, Q. Xie, G. Lu, Y. Wang, D. Luan, X. Tao and X. W. Lou, *Adv. Mater.*, 2022, **34**, 2104405.
46 L. Wu, X. Shen, Z. Ji, J. Yuan, S. Yang, G. Zhu, L. Chen, L. Kong and H. Zhou, *Adv. Funct. Mater.*, 2023, **33**, 2208170.
47 Y. Chen, C. Liu, H. Wang, M. Zhang, C. Li, J. Wu, P. He, W. Fang, W. Fan, C. Yin and L. Sun, *J. Electroanal. Chem.*, 2025, 119053.
48 Y. Guo, C. Zhang, J. Zhang, K. Dastafkan, K. Wang, C. Zhao and Z. Shi, *ACS Sustainable Chem. Eng.*, 2021, **9**, 2047–2056.
49 Y. Qiu, L. Pan, H. Jiang, M. A. Amin and J. Lin, *Nano Res.*, 2025, **18**, 94907019.
50 A. Guđmundsson, K. P. J. Gustafson, B. K. Mai, B. Yang, F. Himo and J.-E. Bäckvall, *ACS Catal.*, 2018, **8**, 12–16.
51 Y. Yang, Q.-N. Yang, Y.-B. Yang, P.-F. Guo, W.-X. Feng, Y. Jia, K. Wang, W.-T. Wang, Z.-H. He and Z.-T. Liu, *ACS Catal.*, 2023, **13**, 2771–2779.
52 J. Zhang, H. Zhang and Y. Huang, *Appl. Catal., B*, 2021, **297**, 120453.
53 J. Zhou, F. Qiao, Z. Ren, X. Hou, Z. Chen, S. Dai, G. Su, Z. Cao, H. Jiang and M. Huang, *Adv. Funct. Mater.*, 2024, **34**, 2304380.
54 T. Bligaard and J. K. Nørskov, *Electrochim. Acta*, 2007, **52**, 5512–5516.
55 C. Wei, Y. Sun, G. G. Scherer, A. C. Fisher, M. Sherburne, J. W. Ager and Z. J. Xu, *J. Am. Chem. Soc.*, 2020, **142**, 7765–7775.
56 J. Zhou, Z. Ren, F. Qiao, H. Gai, S. Qiu, C. Zhang, X. Wang, Z. Chen, H. Jiang and M. Huang, *Appl. Catal., B*, 2024, **353**, 124089.
57 X. Li, M. Chen, Y. Ye, C. Chen, Z. Li, Y. Zhou, J. Chen, F. Xie, Y. Jin, N. Wang and H. Meng, *Small*, 2023, **19**, 2207086.
58 Y. Shi, J. Li, B. Zhang, S. Lv, T. Wang and X. Liu, *Appl. Surf. Sci.*, 2021, **565**, 150506.
59 L. Zhao, J. Yan, H. Huang, X. Du, H. Chen, X. He, W. Li, W. Fang, D. Wang, X. Zeng, J. Dong and Y. Liu, *Adv. Funct. Mater.*, 2024, **34**, 2310902.